

# Experimental and numerical study of the evolution of soot primary particles in a diffusion flame

Maria L. Botero<sup>1</sup>, Nick Eaves<sup>3</sup>, Jochen A.H. Dreyer<sup>3</sup>, Yuan Sheng<sup>2</sup>, Jethro Akroyd<sup>3</sup>, Wenming Yang<sup>1</sup>, Markus Kraft<sup>2</sup>

released: June 21, 2018

<sup>1</sup> Department of Mechanical Engineering  
National University of Singapore  
9 Engineering Drive 1  
117576  
Singapore

<sup>2</sup> School of Chemical and Biomedical Engineering  
Nanyang Technological University  
62 Nanyang Drive  
637459  
Singapore  
E-mail: [mk306@cam.ac.uk](mailto:mk306@cam.ac.uk)

<sup>3</sup> Department of Chemical Engineering  
and Biotechnology  
University of Cambridge  
West Cambridge Site  
Philippa Fawcett Drive  
Cambridge CB3 0AS  
United Kingdom

Preprint No. 202



---

*Keywords:* diffusion flame, soot, particle size distribution, population balance model

**Edited by**

Computational Modelling Group  
Department of Chemical Engineering and Biotechnology  
University of Cambridge  
West Cambridge Site  
Philippa Fawcett Drive  
Cambridge CB3 0AS  
United Kingdom

**Fax:** + 44 (0)1223 334796

**E-Mail:** [c4e@cam.ac.uk](mailto:c4e@cam.ac.uk)

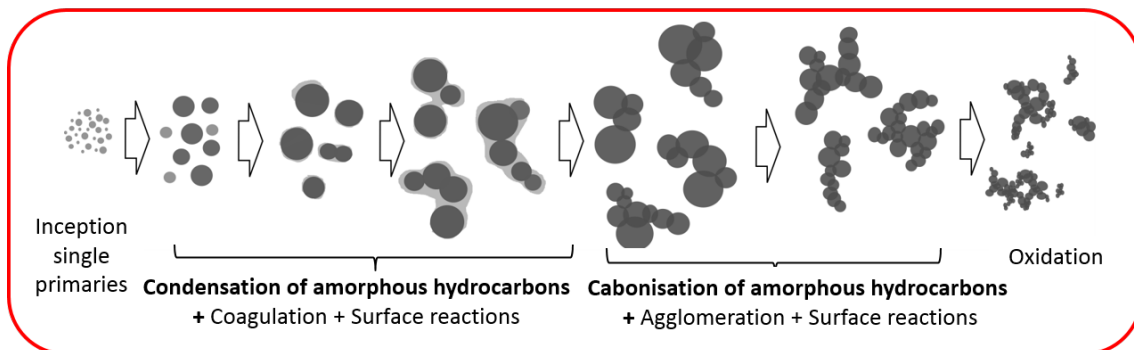
**World Wide Web:** <http://como.cheng.cam.ac.uk/>



## Abstract

The evolution of primary soot particles is studied experimentally and numerically along the centreline of a co-flow laminar diffusion flame. Soot samples from a flame fueled with  $C_2H_4$  are taken thermophoretically at different heights above the burner (HAB), their size and nano-structure are analysed through TEM. The experimental results suggest that after inception, the nascent soot particles coagulate and coalesce to form larger primary particles ( $\sim 5$  to  $15$  nm). As these primary particles travel along the centreline, they grow mainly due to coagulation and condensation and a layer of amorphous hydrocarbons (revealed by HRTEM) forms on their surface. This amorphous layer appears to promote the aggregation of primary particles to form fractal structures. Fast carbonisation of the amorphous layer leads to a graphitic-like shell around the particles. Further graphitisation compacts the primary particles, resulting in a decrease of their size. Towards the flame tip the primary particles decrease in size due to rapid oxidation. A detailed population balance model is used to investigate the mechanisms that are important for prediction of primary particle size distributions. Suggestions are made regarding future model development efforts. Simulation results indicate that the primary particle size distributions are very sensitive to the parameterisation of the coalescence and particle rounding processes. In contrast, the average primary particle size is less sensitive to these parameters. This demonstrates that achieving good predictions for the average primary particle size does not necessarily mean that the distribution has been accurately predicted.

### Primary particle growth model



### Highlights

- Young primary particles have short-range degree of nano-structural order and may possess nano-structural mobility under flame conditions.
- The liquid-like blobs around particles were found to be a sampling artifact.
- Particle growth and agglomeration is largely influenced by the condensation of amorphous hydrocarbons on the primary particles.
- Predicting the average primary particle size does not indicate that the primary particle size distribution is accurately described.

# 1 Introduction

Air pollution from carbon nanoparticles leads to respiratory disease and contributes to climate change. The smallest particles (below 100 nm) play a particularly important role in health since they penetrate the respiratory system deeper than larger particles [4] and dominate size distributions in terms of number concentration. In order to accurately predict the size distributions of soot particles it is necessary to understand the different processes involved in primary particle formation and growth. Numerical models must be able to accurately describe each of these steps to eventually mitigate soot emission.

The inception process, which is the transition from the gas to the first nuclei, is still not completely understood. The smallest particles detected in flames are about 1–3 nm in diameter [1, 40, 46] and are thought to consist of PAH clusters [24] with 10–15 aromatic rings [2, 9, 10, 36]. It is unclear whether these particles are nascent soot particles [5, 46] or soot precursor particles [13, 15]. These last ones have been found transparent to visible light [13] and sometimes they are described as “liquid-like” when observed under transmission electron microscopy (TEM), due to their low contrast [14, 17, 31], undefined boundaries and their deformation during thermophoretic sampling [1, 3, 29]. Recently, some researchers have been able to detect and measure these nascent soot particles using advanced techniques [5, 40, 46].

Laminar co-flow diffusion flames have been used extensively to study soot formation because they represent a simple analogue of more complex practical combustion systems. In these flames, the transition from precursor particles into solid nuclei is also debated. Some researchers have reported that the polydisperse precursor particles coagulate fast to form larger primary particles [13] and then carbonise [32] into solid monodisperse spherical particles via a mechanism that includes surface growth. The solid particles then aggregate to form larger fractal structures. Others reported the partial aggregation of the precursor particles before their complete solidification [31, 49]. Small solid nuclei form within large PAH-containing liquid-like particles [29, 31, 43], through carbonisation these liquid-like particles rapidly convert into small aggregates composed of mature primary particles [29] and further agglomerate to form larger fractal structures. Due to the complexity of the multiple processes that are taking place simultaneously in the flame, it is not yet possible to reconcile fully the influence of each process with experimental observations of the growth of primary particles.

Several modeling studies in co-flow diffusion flames have been reported in the past 20 years. The majority of these investigations used population balance models (PBM) that describe particles by one or two parameters (mass and number of primary particles or surface and volume) that are solved via sectional or moment methods. Two parameter models allow for a description of the fractal nature of soot aggregates; however, information regarding the primary particle size distribution (PPSD) within aggregates cannot be obtained. Previous numerical studies have focused on prediction of average primary particle size, partially due to the lack of experimental data on their number and size distributions, but also due to the limitations of the soot models implemented [37].

Herein, experimental and detailed modeling of the evolution of the primary particles of soot in a laminar diffusion flame of ethylene, is presented. The flame corresponds to one

of the target flames defined at the International Sooting Flame (ISF) workshop for soot studies [50]. To the author’s knowledge, this is the first time that experimental and simulated PSD in a co-flow diffusion flame are reported. The presented methodology can be extended to other reactive flows. The growth of primary particles from single nascent precursor to mature particles in large aggregates is observed using TEM and simulated using a population balance model with a detailed description of the molecular and morphological structure of each particle (DPBM) [45, 51] and capable of resolving primary particle distributions within soot aggregates. Through the unique features of the soot model, a parametric sensitivity analysis is performed to challenge the understanding of the role of various particle processes in the evolution of the soot primary particle size in the flame. Raw experimental data is provided in the supplementary material data to ease future modeling efforts by the community.

## 2 Experimental methods

The Yale burner [25] was used to generate a co-flow diffusion flame of ethylene diluted by nitrogen (60% vol C<sub>2</sub>H<sub>4</sub> - 40% vol N<sub>2</sub>), which corresponds to the ISF-3 Co-flow 3c [50]. Soot was sampled at different height above the burner (HAB) in the centreline using a fast-insertion thermophoretic sampling system [10]. For all the sampling positions, the exposure of the TEM grids was between 30-46 ms. Carbon-supported copper grids with a diameter of 3.05 mm were used to collect the soot samples. The samples were examined on a 200 kV JEOL 2100F TEM using a ZrO/W Schottky field emission gun. TEM images were taken with a magnification of 30,000x and 500,000x. The primary particle size was measured by fitting circles around the particles on each TEM image using a MATLAB code. More than 1000 primary particles were analysed at each sampling position. Contamination of the sample from large wing aggregates was estimated to be ±15%. The flame temperature was measured with an uncoated R-type thermocouple with a wire diameter of 75 μm and corrected for radiation losses as detailed in [8]. Full details of the burner and sampling conditions can be found in the supplementary material.

## 3 Numerical Methods

The computational method consists of two parts as in previous studies. In the first part, velocity, and species profiles are computed using the CoFlame code, which includes a sectional description of the soot particle distribution and considers particle mass and number of primaries. The chemical mechanism in [18] is utilized along with PAH inception and condensation via benzo-a-pyrene (A5) [21], which is the largest PAH considered in the mechanism. The details of the CoFlame code can be found in [22] and previous works [19, 20, 23, 30].

In the second part, a streamline corresponding to the centreline of the diffusion flame is generated from the CoFlame results and a detailed PBM is applied as a post-processing step. The post-processing methodology is well established and has been applied in a number of previous studies [12, 52, 53], although it should be noted that it cannot account for

the effect of thermophoresis or diffusion of the particles. The experimental temperature profile is supplied as input along with shifting the profiles from the CoFlame code by 5 mm to match the experimental flame height. A brief description of the most important aspects of the detailed PBM is given below. Full details may be found elsewhere [12, 42, 45, 53]. The growth of PAH species within the model is described by a kinetic Monte-Carlo-aromatic-site (KMC-ARS) model [42], starting from benzo-a-pyrene. The dynamics of the soot particle population is described by the Smoluchowski equation with additional terms for particle inception, surface growth, oxidation, condensation, particle rounding, and sintering. In the model, soot particles are represented as aggregates composed of primary particles, where each primary particle is composed of a number of PAHs [45]. A PAH is represented by the number of carbon and hydrogen atoms it contains, and the number and types of elementary sites on its edge [42]. Each aggregate stores a list of neighbouring primary particles and resolves the common surface area between each pair of neighbours, where each pair of neighbours can be in point contact, can be fully coalesced or can be anywhere in between [45]. The extent of contact between neighboring particles is described by a sintering level [44]. A sintering level of 0 corresponds to point contact. A sintering level of 1 corresponds to complete coalescence. The sintering level is increased via sintering and particle rounding processes. Sintering is modeled via the viscous flow model and is parametrised based on a pre-exponential factor  $A_s$ , activation energy  $E_a$ , and the critical diameter below which primaries are assumed to have nanostructural mobility ("liquid-like") and sinter instantaneously (coalescence),  $d_{p,crit}$ . Particle rounding is the increase of sintering level due to condensation and surface growth reactions and is parameterised by the smoothing factor,  $\sigma$ . A value of 0 implies no rounding, while a value of 2 implies maximum rounding. A list of all the parameters utilized with the model can be found in the supplementary material.

## 4 Results and Discussion

### 4.1 Flame temperature

Experimental and simulated temperature profiles at the centreline are presented in **Fig. 1**. The experimental temperature profile and maximum temperature measured in this study are consistent with the data reported by Smooke et al. [47]. However, our experimental results are slightly shifted towards higher HAB, possibly due to the definition of the zero HAB and the difficulties to insert the thermocouple very close to the burner rim. At low HAB, the predicted temperature is significantly lower than the measurements, which was also reported for previous modeling efforts of this flame [48]. The simulated peak temperature is 100 K larger and is also shifted to larger HAB. The simulated temperature profile was then shifted by -5 mm in order to match the HAB at which the maximum temperature is obtained, resulting in a better agreement between the computations and experiments.

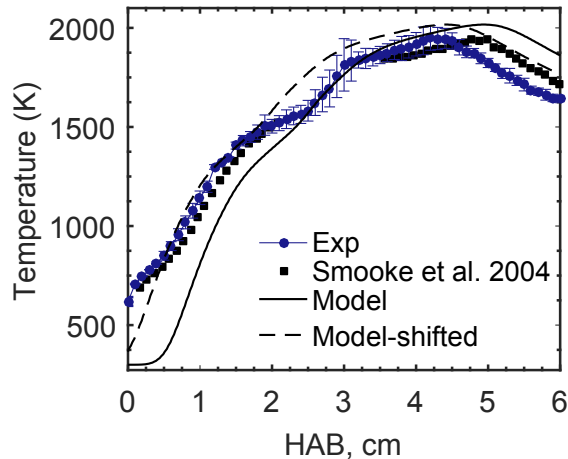


**Figure 1:** *Temperature profile at the centreline of the flame. Experimental and numerical results.*

## 4.2 Soot morphology

The evolution of soot morphology along the flame centreline is presented in **Figure 2** including the mean primary particle diameter  $\langle d_{pp} \rangle$  and estimated standard error. Soot is first detected at 10 mm HAB and consists of small single particles with an average size of 11 nm. The smallest particles that could be detected were between 4-5 nm. A small degree of aggregation is observed with almost complete coalescence, indicating that these particles may be formed from the coalescence of smaller particles [38, 39]. Some of these nascent particles have low contrast and blurred boundaries whereas others present high-contrast and well-defined boundaries. HRTEM images reveal that they exhibit a short-range degree of nano-structural order and also a slight spreading on the substrate film (**Figure 3**).

Downstream (16 to 20 mm HAB), the primary particles grow to sizes between 13 nm and 25 nm and consist mostly of single particles with some initial signs of aggregation. Different degrees of contrast are also observed, some of them present the low-contrast reported by other researchers as “transparent-like”, and some present a high contrast associated with solid particles. High resolution images of these particles show that they possess a higher degree of nano-structural order (**Figure 3**). We do not assume these particles to be true liquids, but only that they possess some nano-structural mobility under flame conditions [26].

At 25 mm HAB (and to a lesser extent at 20 mm HAB) the aggregates have irregular shapes with a combination of well-defined spherical-like primaries and irregular structures. HRTEM images of these particles show that they consist of soot particles with some graphitic order surrounded by a layer of an amorphous carbon material. This explains the lower contrast of the particles on the edges and joints [6] (**Figure 4**). Chemical speciation of incipient soot particles with similar morphology was performed by Blevins et al. [6], Öktem et al. [41], using laser desorption and solvent extraction followed by mass spectrometry. Their results show that the species desorbed from the particles are mainly composed of small PAHs (3-5 rings) and aliphatic molecules. The HRTEM images reveal



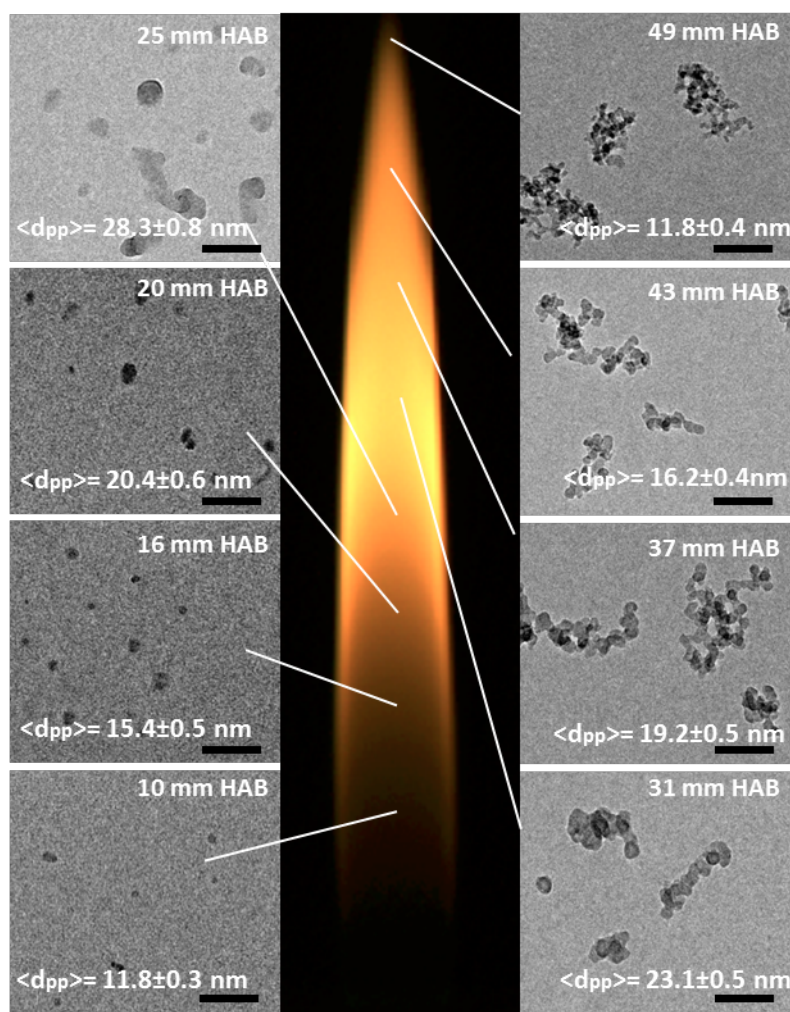


**Figure 2:** Representative TEM images showing the evolution of soot morphology in the flame. Left: soot images at low-medium HAB, Right: soot images at medium-large HAB. Each image contains the mean primary particle diameter at the corresponding HAB. Scale bar of 100 nm.

that the small nascent primary particles at low HAB do not have the same nanostructure as the amorphous (“liquid-like”) carbon condensed around the larger primaries at intermediate HAB.

Liquid-like patches surrounding the particles were observed at intermediate HAB (25 mm) and were found to be dependent on the sampling time (images can be found in the supplementary material), as reported by Kholghy et al. [29]. As the exposure time of the TEM grid to the flame decreases, these liquid-like blobs become smaller until they disappear, suggesting less condensation of hydrocarbons with high boiling points on the sampling grid [6]. In our measurements, it was possible to avoid this condensable material with sufficiently short exposure times.

Further downstream, at 31 mm HAB larger aggregates with high-contrast and well-defined spherical shape are found. HRTEM images at this HAB (Figure 5) evidence the fast



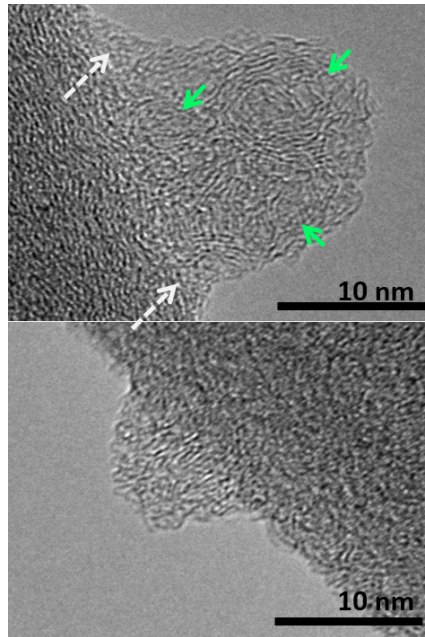


**Figure 3:** Representative HRTEM images of smallest soot particles sampled at 10 mm HAB, showing a short-range nano-structural order and internal nano-structures of smaller nascent particles (green arrows). Slight spreading can be observed in the edges of particle-grid contact (white-dashed arrows).

graphitisation of the previously condensed amorphous layer, forming a graphitic-like layer around the particles, probably due to the higher flame temperatures [29]. A slight decrease in the primary particle size is encountered suggesting a decrease in surface growth and compaction of the primary particles triggered by the increase in graphitisation [16, 29, 49]. Towards the top of the flame, the aggregate size remains fairly constant whilst the primary particle size consistently decreases. At the tip of the flame, both aggregate and primary particle size decrease substantially, due to soot oxidation [7, 11, 28, 35].

### 4.3 Primary particle size distribution

Experimental and simulated PPSDs at different HAB are presented in **Figure 6**. A kernel density estimation was used to generate the probability distribution function using a bandwidth of 2 nm. The detection limit in the experimental data is approximately 4 nm for single primaries (due to the poor contrast). Experimental results show that the PPSD shifts progressively to larger sizes and becomes wider from 10 to 25 mm HAB due to a combination of growth processes, then it shifts back to smaller sizes and narrows from 31 to 49 mm HAB due to combined graphitisation and oxidation. At all HAB, the PPSD is unimodal with a narrow width. At 25 mm HAB a second mode of large particles slightly emerges; however, at this HAB the spherical primary particle size measured cannot fully represent the complex morphology of the aggregates described in the previous section.

There are many hypothesised mechanisms that contribute to the growth of primary parti-

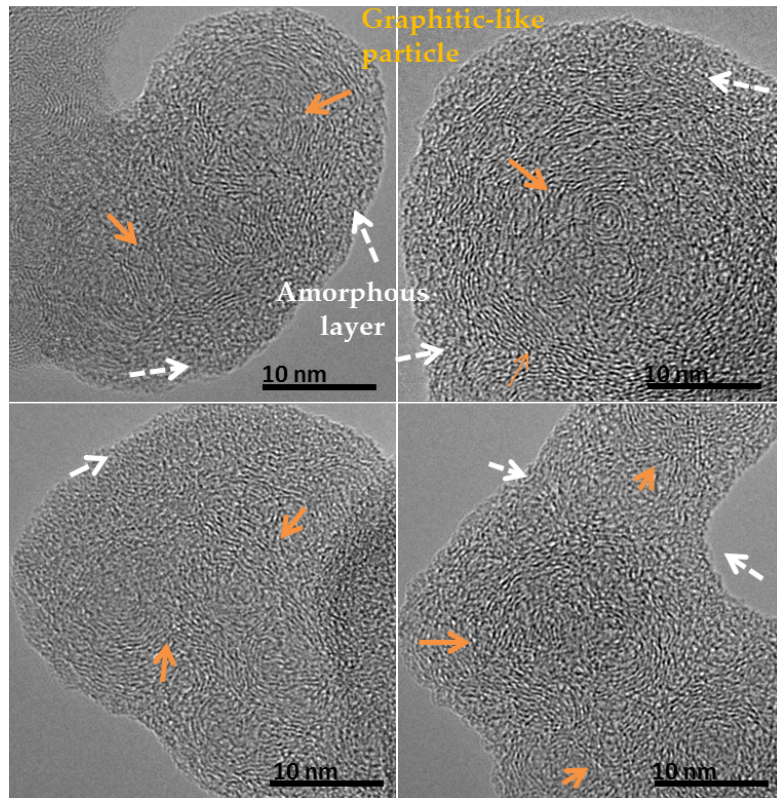


**Figure 4:** HRTEM images of soot sampled at 25 mm HAB showing existence of an amorphous carbon layer (white dashed arrow) surrounding the semi-graphitic solid particles (orange arrows).

cles, such as sintering, particle rounding, and coalescence of liquid particles, all of which are described in the detailed PBM. This is the first time experimental data for the full PPSD is available, which allows the use of the PBM to challenge the accepted hypotheses. A sensitivity analysis is performed in order to understand the mechanisms that are important to the prediction of primary particle sizes and their contributions. The parameters that are investigated are 1) the sintering pre-factor ( $A_s$ ), 2) critical diameter for instantaneous coalescence  $d_{\text{pri,crit}}$ , and 3) the smoothing factor ( $\sigma$ ). Table 1 lists the parameters for each trial.

Before moving to the PPSDs, the commonly investigated average primary particle size and standard deviation are briefly discussed. **Figure 7** displays the experimental and numerical results for average primary particle size and standard deviation versus HAB (to be consistent with experimental limitations, only simulated particles larger than 4 nm were included). The numerical results show modest sensitivity to the investigated parameters when considering the average size, whereas the standard deviation is more sensitive.

Although the model is capable of reasonably reproducing the trends in average size, it does not capture the experimental PPSD. In **Figure 6**, simulated PPSD results of selected trials are compared with experimental results. Results of all the trials can be found in the supplementary material. At all HABs, the numerical results exhibit a large mode of sub 2 nm primary particles. Additionally, results are shifted towards larger sizes and display a

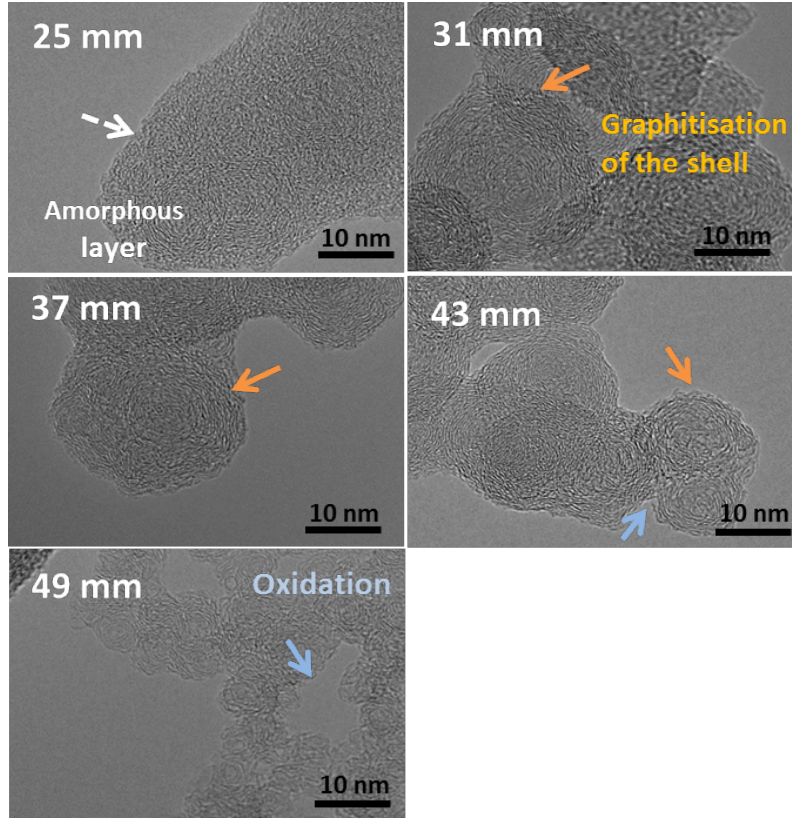


**Figure 5:** Representative HRTEM images of soot sampled at the flame centreline showing the evolution of the nano-structure of soot primary particle during growth and oxidation.

**Table 1:** Parameters for each trial run for the detailed population balance model (DPBM).

| Trial | $A_s$ ( $\text{s m}^{-1}$ ) | $d_{p,\text{crit}}$ (nm) | $\sigma$ |
|-------|-----------------------------|--------------------------|----------|
| 1     | $1.1 \times 10^{-14}$       | 1.58                     | 1.69     |
| 2     | $1.1 \times 10^{-13}$       | 1.58                     | 1.69     |
| 3     | $1.1 \times 10^{-12}$       | 1.58                     | 1.69     |
| 4     | $1.1 \times 10^{-14}$       | 3                        | 1.69     |
| 5     | $1.1 \times 10^{-14}$       | 5                        | 1.69     |
| 6     | $1.1 \times 10^{-14}$       | 1.58                     | 1.0      |
| 7     | $1.1 \times 10^{-14}$       | 1.58                     | 0.5      |

multi-modal character at higher HAB. The PPSDs show marked, and differing, sensitivity to all investigated parameters:

- Reducing the sintering pre-factor (Trials 2 and 3, see Fig. S3) reduces the multimodality at large HAB and causes the predicted PPSDs to become uni-modal. A very large sintering pre-factor results in the complete coalescence of sticking

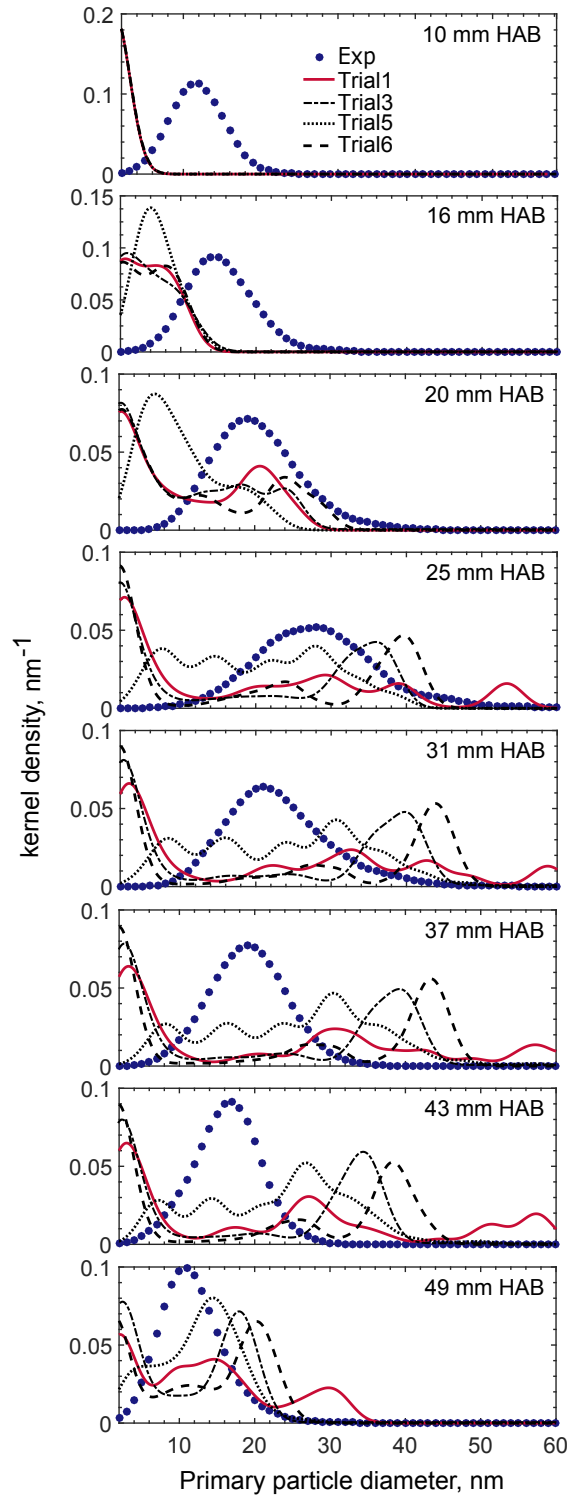


**Figure 6:** *Experimental and simulated primary particle size distribution at different HAB. Trial 1: base case, Trial 3: reduce sintering pre-factor, Trial 5: increase coalescence critical diameter, Trial 6: reduce smoothing factor*

primary particles, resulting in the rapid transition of aggregates back to spherical

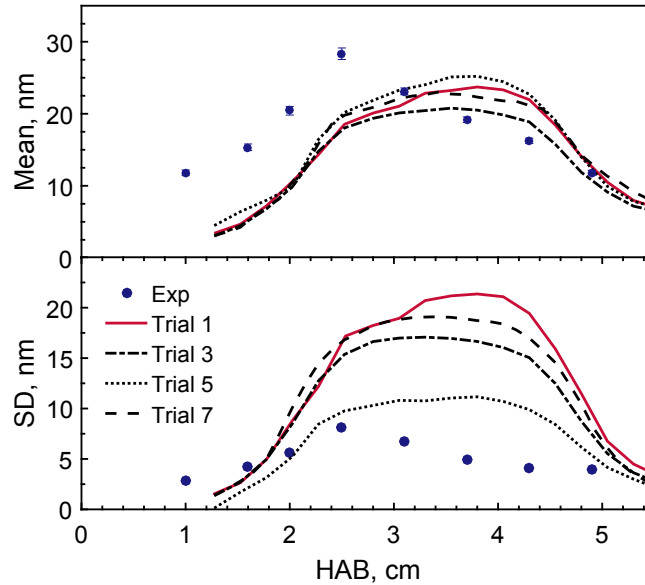


**Figure 7:** (a) Mean and (b) standard deviation of primary particle size at different HAB. Comparison of experimental and simulation results.

particles of equivalent mass, which increases the multimodality of the PPSD. A low sintering pre-factor would prevent particles from merging, such that they persist as aggregates. The experimental evidence suggests that sintering should be strong in the inception region and decrease as the particles travel through the flame.

- Increasing the critical diameter for coalescence,  $d_{p,crit}$  (Trials 4 and 5, see Fig. S4a), eliminates the larger mode of sub 2 nm primaries and the modes at larger primary particle sizes at high HAB. This parameter represents the nano-structural mobility exhibited by nascent soot particles (so called “liquid-like” behavior in the literature), which facilitates their coalescence with larger particles.
- Reductions in the smoothing factor (Trials 6 and 7, see Fig. S4b) causes the predicted PPSDs to become bi- rather than multi-modal. The smoothing factor controls the rate of rounding due to molecules sticking to the particle surface. Thus, if it is too high, every surface growth reaction or condensation event would result in the complete rounding of neighbour particles into an spherical primary particle, resulting in a multi-modal PPSD. If the smoothing factor is too low, condensation and surface reactions would lead only to surface growth of the primary particle where the event takes place. This reduces the multimodality and allows the particles to remain as aggregates; however, it promotes the preferential surface growth of some particles, leading to a bi-modal distribution with a very pronounced mode of large primary particles.

Overall, these results display that while multiple hypotheses of the contributions of various mechanisms can provide reasonable, and similar, results for average size, the same is not true regarding the PPSD. A summary of the influence of the model parameters on the predicted PPSDs is show in **Figure 8**. It is important to highlight that this is the first attempt to use a detailed model that resolves the connections between individual primary



particles to test hypotheses about the processes involved in the formation and aggregation of primary particles. The experimental observations presented in this paper enables such models to be challenged and define specific aspects for future development.

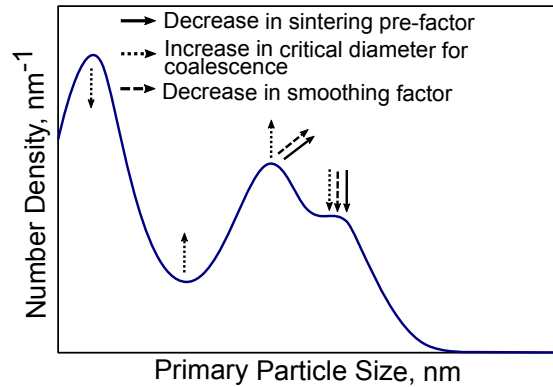


**Figure 8:** Summary of effects of key model parameters on predicted primary particle size distributions (PPSDs).

## 5 Conclusions

The evolution of the primary particle size distribution (PPSD) of soot in a co-flow diffusion flame was investigated experimentally and numerically, for the first time. Experimental results show that the smallest soot particles detected (4-5 nm) are formed by the coalescence of smaller nascent soot particles. These primary particles grow in size through coagulation and surface growth (including condensation of small hydrocarbon species). The amorphous hydrocarbons condensed on the particle surface hereby seem to aid the aggregation process. We do not assume these particles to be true liquids, but rather that their surface possesses some nano-structural mobility under flame conditions. The amorphous layer graphitise due to the higher flame temperatures and starts forming a graphitic-like layer around the particles as evidenced by HRTEM images. Towards the flame tip the particles are oxidised. The experimental PPSD is mono-modal at all HAB with a narrow width. During the growth of particles the PPSD shifts to larger sizes and widens. During the shrinkage of particles, the PPSD shifts to smaller sizes and narrows. The predicted PPSDs by the detailed PBM are sensitive to the sintering pre-factor, critical diameter for “liquid-like” behavior, and smoothing factor, while average sizes are not sensitive. This demonstrates that reasonable prediction of average sizes does not ensure reasonable prediction of the distribution.

## 6 Acknowledgments

This project is funded by the National Research Foundation (NRF), Prime Minister’s Office, Singapore under its Campus for Research Excellence and Technological Enterprise (CREATE) programme.

## References

- [1] A. Abid, N. Heinz, E. Tolmachoff, D. Phares, C. Campbell, and H. Wang. On evolution of particle size distribution functions of incipient soot in premixed ethylene-oxygen-argon flames. *Combustion and Flame*, 154:775–788, 2008.
- [2] E. M. Adkins and J. H. Miller. Extinction measurements for optical band gap determination of soot in a series of nitrogen-diluted ethylene/air non-premixed flames. *Physical Chemistry Chemical Physics*, 17:2686–2695, 2015. doi:10.1039/C4CP04452E.
- [3] A. C. Barone, A. D. Alessio, and A. D’Anna. Morphological characterization of the early process of soot formation by atomic force microscopy. *Combustion and Flame*, 132:181–187, 2003.
- [4] K. BéruBé, D. Balharry, K. Sexton, L. Koshy, and T. Jones. Combustion-derived nanoparticles: Mechanisms of pulmonary toxicity. *Clinical and Experimental Pharmacology and Physiology*, 34(10):1044–1050, 2007. ISSN 1440-1681. doi:10.1111/j.1440-1681.2007.04733.x.
- [5] C. Betrancourt, F. Liu, P. Desgroux, X. Mercier, A. Faccinetto, M. Salamanca, L. Ruwe, K. Kohse-Höinghaus, D. Emmrich, A. Beyer, A. Gölzhäuser, and T. Tritscher. Investigation of the size of the incandescent incipient soot particles in premixed sooting and nucleation flames of n-butane using lii, him, and 1 nm-smtps. *Aerosol Science and Technology*, 51(8):916–935, 2017. doi:10.1080/02786826.2017.1325440.
- [6] L. G. Blevins, R. a. Fletcher, B. a. Benner, E. B. Steel, and G. W. Mulholland. The existence of young soot in the exhaust of inverse diffusion flames. *Proceedings of the Combustion Institute*, 29(2):2325–2333, jan 2002. ISSN 15407489. doi:10.1016/S1540-7489(02)80283-8.
- [7] M. L. Botero, S. Mosbach, and M. Kraft. Sooting tendency of paraffin components of diesel and gasoline in diffusion flames. *Fuel*, 126:8 – 15, 2014. ISSN 0016-2361. doi:10.1016/j.fuel.2014.02.005.
- [8] M. L. Botero, S. Mosbach, J. Akroyd, and M. Kraft. Sooting tendency of surrogates for the aromatic fractions of diesel and gasoline in a wick-fed diffusion flame. *Fuel*, 153:31 – 39, 2015. ISSN 0016-2361. doi:10.1016/j.fuel.2015.02.108.
- [9] M. L. Botero, E. M. Adkins, S. González-Calera, H. Miller, and M. Kraft. PAH structure analysis of soot in a non-premixed flame using high-resolution transmission electron microscopy and optical band gap analysis. *Combustion and Flame*, 164:250–258, 2016. ISSN 00102180. doi:10.1016/j.combustflame.2015.11.022.



- [10] M. L. Botero, D. Chen, S. González-Calera, D. Jefferson, and M. Kraft. HRTEM evaluation of soot particles produced by the non-premixed combustion of liquid fuels. *Carbon*, 96:459–473, 2016. ISSN 00086223. doi:10.1016/j.carbon.2015.09.077.
- [11] M. L. Botero, S. Mosbach, and M. Kraft. Sooting tendency and particle size distributions of n-heptane/toluene mixtures burned in a wick-fed diffusion flame. *Fuel*, 169 (Supplement C):111 – 119, 2016. ISSN 0016-2361. doi:10.1016/j.fuel.2015.12.014.
- [12] D. Chen, Z. Zainuddin, E. Yapp, J. Akroyd, S. Mosbach, and M. Kraft. A fully coupled simulation of PAH and soot growth with a population balance model. *Proceedings of the Combustion Institute*, 34(1):1827 – 1835, 2013. ISSN 1540-7489. doi:10.1016/j.proci.2012.06.089.
- [13] A. D’Anna, A. Rolando, C. Allouis, P. Minutolo, and A. D’Alessio. Nano-organic carbon and soot particle measurements in a laminar ethylene diffusion flame. *Proceedings of the Combustion Institute*, 30(1):1449 – 1456, 2005. ISSN 1540-7489. doi:https://doi.org/10.1016/j.proci.2004.08.276.
- [14] A. D’Anna, A. Ciajolo, M. Alfè, B. Apicella, and A. Tregrossi. Effect of fuel/air ratio and aromaticity on the molecular weight distribution of soot in premixed n-heptane flames. *Proceedings of the Combustion Institute*, 32(1):803 – 810, 2009. ISSN 1540-7489. doi:10.1016/j.proci.2008.06.198.
- [15] S. Di Stasio, J. B. a. Mitchell, J. L. Legarrec, L. Biennier, and M. Wulff. Synchrotron SAXS <in situ> identification of three different size modes for soot nanoparticles in a diffusion flame. *Carbon*, 44(7):1267–1279, 2006. doi:10.1016/j.carbon.2005.10.042.
- [16] R. Dobbins. Hydrocarbon nanoparticles formed in flames and diesel engines. *Aerosol Science and Technology*, 41(5):485–496, 2007. ISSN 02786826. doi:10.1080/02786820701225820.
- [17] R. Dobbins, R. Fletcher, and H.-C. Chang. The evolution of soot precursor particles in a diffusion flame. *Combustion and Flame*, 115(3):285–298, nov 1998. ISSN 00102180. doi:10.1016/S0010-2180(98)00010-8.
- [18] S. B. Dworkin, Q. Zhang, M. J. Thomson, N. A. Slavinskaya, and U. Riedel. Application of an enhanced pah growth model to soot formation in a laminar coflow ethylene/air diffusion flame. *Combustion and Flame*, 158(9):1682–1695, 2011.
- [19] N. A. Eaves, A. Veshkini, C. Riese, Q. Zhang, S. B. Dworkin, and M. J. Thomson. A numerical study of high pressure, laminar, sooting, ethane-air coflow diffusion flames. *Combustion and Flame*, 159(10):3179–3190, 2012.
- [20] N. A. Eaves, M. J. Thomson, and S. B. Dworkin. The effect of conjugate heat transfer on soot formation modelling at elevated pressures. *Combustion Theory and Modelling*, 185(12):1799–1819, 2013.

- [21] N. A. Eaves, S. B. Dworkin, and M. J. Thomson. The importance of reversibility in modeling soot nucleation and condensation processes. *Proceedings of the Combustion Institute*, 35(2):1787–1794, 2015.
- [22] N. A. Eaves, Q. Zhang, F. Liu, H. Guo, S. B. Dworkin, and M. J. Thomson. Coflame: A refined and validated numerical algorithm for modeling sooting laminar coflow diffusion flames. *Computer Physics Communications*, 207:464–477, 2016.
- [23] N. A. Eaves, S. B. Dworkin, and M. J. Thomson. Assessing relative contributions of paths to soot mass by reversible heterogeneous nucleation and condensation. *Proceedings of the Combustion Institute*, 36(1):935–945, 2017.
- [24] P. Elvati and A. Violi. Thermodynamics of poly-aromatic hydrocarbon clustering and the effects of substituted aliphatic chains. *Proceedings of the Combustion Institute*, 34(1):1837 – 1843, 2013. ISSN 1540-7489. doi:10.1016/j.proci.2012.07.030.
- [25] J. Gau, D. Das, C. McEnally, D. Giassi, N. Kempema, and M. Long. Yale coflow diffusion flames steady flame burner. [http://guilford.eng.yale.edu/yalecoflowflames/steady\\_burner.html](http://guilford.eng.yale.edu/yalecoflowflames/steady_burner.html).
- [26] R. H. Hurt, G. P. Crawford, and H.-S. Shim. Equilibrium nanostructure of primary soot particles. 28:2539–2546, 2000.
- [27] N. J. Kempema and M. B. Long. Combined optical and {TEM} investigations for a detailed characterization of soot aggregate properties in a laminar coflow diffusion flame. *Combustion and Flame*, 164:373 – 385, 2016. ISSN 0010-2180. doi:10.1016/j.combustflame.2015.12.001.
- [28] I. M. Kennedy. Models of soot formation and oxidation. *Progress in Energy and Combustion Science*, 23(2):95–132, 1997. ISSN 03601285. doi:10.1016/S0360-1285(97)00007-5.
- [29] M. Kholghy, M. Saffaripour, C. Yip, and M. J. Thomson. The evolution of soot morphology in a laminar coflow diffusion flame of a surrogate for Jet A-1. *Combustion and Flame*, 160(10):2119–2130, 2013. ISSN 00102180. doi:10.1016/j.combustflame.2013.04.008.
- [30] A. Khosousi, F. Liu, S. B. Dworkin, N. A. Eaves, M. J. Thomson, X. He, Y. Dai, Y. Gao, F. Liu, S. Shuai, and J. Wang. Experimental and numerical study of soot formation in laminar coflow diffusion flames of gasoline/ethanol blends. *Combustion and Flame*, 162(10):3925–3933, 2015.
- [31] U. O. Koylu, C. S. McEnally, D. E. Rosner, and L. D. Pfefferle. Simultaneous Measurements of Soot Volume Fraction and Particle Size / Microstructure in Flames Using a Thermophoretic Sampling Technique. *Combustion and Flame*, 110:494–507, 1997.
- [32] J. Lahaye, G. Prado, J. B. Donnet, and I. M. Kennedy. NUCLEATION AND GROWTH OF CARBON BLACK PARTICLES DURING THERMAL DECOMPOSITION OF BENZENE. *Carbon*, 12(1):27–35, 1974. doi:10.1016/0008-6223(74)90037-2.

- [33] J. Lee and S. Y. Yang. A study of stability and vibration for particle sampling probes. *International Journal of Mechanical Sciences*, 76(Supplement C):152 – 157, 2013. ISSN 0020-7403. doi:10.1016/j.ijmecsci.2013.09.013.
- [34] J. Lee, I. Altman, and M. Choi. Design of thermophoretic probe for precise particle sampling. *Journal of Aerosol Science*, 39(5):418 – 431, 2008. ISSN 0021-8502. doi:10.1016/j.jaerosci.2008.01.001.
- [35] Z. Li, L. Qiu, X. Cheng, Y. Li, and H. Wu. The evolution of soot morphology and nanostructure in laminar diffusion flame of surrogate fuels for diesel. *Fuel*, 211 (Supplement C):517 – 528, 2018. ISSN 0016-2361. doi:10.1016/j.fuel.2017.09.036.
- [36] J. Lighty, V. Romano, A. Sarofim, H. Bockhorn, A. D’Anna, A. Sarofim, and H. Wang. Combustion generated fine carbonaceous particles. *Combustion Generated Fine Carbonaceous Particles*, KIT Scientific Publishing, pages 487–500, 2009.
- [37] W. J. Menz and M. Kraft. The suitability of particle models in capturing aggregate structure and polydispersity. *Aerosol Science and Technology*, 47(7):734–745, 2013. doi:10.1080/02786826.2013.788244.
- [38] P. A. Mitchell and M. Frenklach. Monte Carlo simulation of soot aggregation with simultaneous surface growth. Ph.D.:317 p., 2001.
- [39] N. Morgan, M. Kraft, M. Balthasar, D. Wong, M. Frenklach, and P. Mitchell. Numerical simulations of soot aggregation in premixed laminar flames. *Proceedings of the Combustion Institute*, 31(1):693 – 700, 2007. ISSN 1540-7489. doi:10.1016/j.proci.2006.08.021.
- [40] T. Mouton, X. Mercier, M. Wartel, N. Lamoureux, and P. Desgroux. Laser-induced incandescence technique to identify soot nucleation and very small particles in low-pressure methane flames. *Applied Physics B*, 112(3):369–379, Sep 2013. ISSN 1432-0649. doi:10.1007/s00340-013-5446-x.
- [41] B. Öktem, M. P. Tolocka, B. Zhao, H. Wang, and M. V. Johnston. Chemical species associated with the early stage of soot growth in a laminar premixed ethylene - oxygen - argon flame. *Combustion and Flame*, 142(4):364 – 373, 2005. ISSN 0010-2180. doi:10.1016/j.combustflame.2005.03.016.
- [42] A. Raj, M. Celnik, R. Shirley, M. Sander, R. Patterson, R. West, and M. Kraft. A statistical approach to develop a detailed soot growth model using PAH characteristics. *Combustion and Flame*, 156(4):896 – 913, 2009. ISSN 0010-2180. doi:10.1016/j.combustflame.2009.01.005.
- [43] P. T. A. Reilly, R. A. Gieray, W. B. Whitten, and J. M. Ramsey. Direct observation of the evolution of the soot carbonization process in an acetylene diffusion flame via real-time aerosol mass spectrometry. *Combustion and Flame*, 122(1-2):90–104, 2000. ISSN 00102180. doi:10.1016/S0010-2180(00)00105-X.
- [44] M. Sander, R. H. West, M. S. Celnik, and M. Kraft. A detailed model for the sintering of polydispersed nanoparticle agglomerates. *Aerosol Science and Technology*, 43 (10):978–989, 2009.

- [45] M. Sander, R. I. Patterson, A. Braumann, A. Raj, and M. Kraft. Developing the PAH-PP soot particle model using process informatics and uncertainty propagation. *Proceedings of the Combustion Institute*, 33(1):675 – 683, 2011. ISSN 1540-7489. doi:10.1016/j.proci.2010.06.156.
- [46] M. Schenk, S. Lieb, H. Vieker, A. Beyer, A. Gölzhäuser, H. Wang, and K. Kohse-Höinghaus. Imaging nanocarbon materials: Soot particles in flames are not structurally homogeneous. *ChemPhysChem*, 14(14):3248–3254, 2013. ISSN 1540-7489. doi:10.1002/cphc.201300581.
- [47] M. D. Smooke, R. J. Hall, M. B. Colket, J. Fielding, M. B. Long, C. S. McEnally, and L. D. Pfefferle. Investigation of the transition from lightly sooting towards heavily sooting co-flow ethylene diffusion flames. *Combustion Theory and Modelling*, 8 (July 2014):593–606, 2004. ISSN 1364-7830. doi:10.1088/1364-7830/8/3/009.
- [48] M. D. Smooke, M. B. Long, B. C. Connelly, M. B. Colket, and R. J. Hall. Soot formation in laminar diffusion flames. *Combustion and Flame*, 143(4):613–628, 2005.
- [49] R. L. V. Wal. Onset of Carbonization: Spatial Location Via Simultaneous LIF-LII and Characterization Via TEM. *Combustion Science and Technology*, 118(4-6):343–360, 1996. ISSN 0010-2202. doi:10.1080/00102209608951985.
- [50] I. S. F. Workshop. Laminar flames - co-flow laminar diffusion flame. <https://www.adelaide.edu.au/cet/isfworkshop/data-sets/laminar/>, 2017.
- [51] E. K. Y. Yapp and M. Kraft. *Modelling Soot Formation: Model of Particle Formation*, pages 389–407. Springer London, London, 2013. ISBN 978-1-4471-5307-8.
- [52] E. K. Y. Yapp, D. Chen, J. Akroyd, S. Mosbach, M. Kraft, J. Camacho, and H. Wang. Numerical simulation and parametric sensitivity study of particle size distributions in a burner-stabilised stagnation flame. *Combustion and Flame*, 162(6):2569–2581, 2015.
- [53] E. K. Y. Yapp, R. I. A. Patterson, J. Akroyd, S. Mosbach, E. M. Adkins, J. Houston Miller, and M. Kraft. Numerical simulation and parametric sensitivity study of optical band gap in a laminar co-flow ethylene diffusion flame. *Combustion and Flame*, 167:320–334, 2016.

# Supplemental Material

## A Experimental methodology

### A.1 Burner

The burner consists of a central fuel tube with an inner diameter of 4 mm and a concentric air co-flow tube with an inner diameter of 7 mm. The fuel velocity at the burner surface had a parabolic profile and the air coflow was plug flow produced by a honeycomb on top, both with an average velocity of 35 cm/s [47]. The fuel, nitrogen and air flow rates are 134.7 ml/min ( $\pm 1\%$ ), 91.2 ml/min ( $\pm 1\%$ ) and 89.1 l/min ( $\pm 2\%$ ) respectively, set by Vögtlin Red-Y digital flow controllers. The visible flame height is approximately 50 mm from the fuel tube exit. The burner is mounted on a motorized translational stage that moves it both horizontally and vertically. An schematic of the burner is presented in **Figure S1a**.

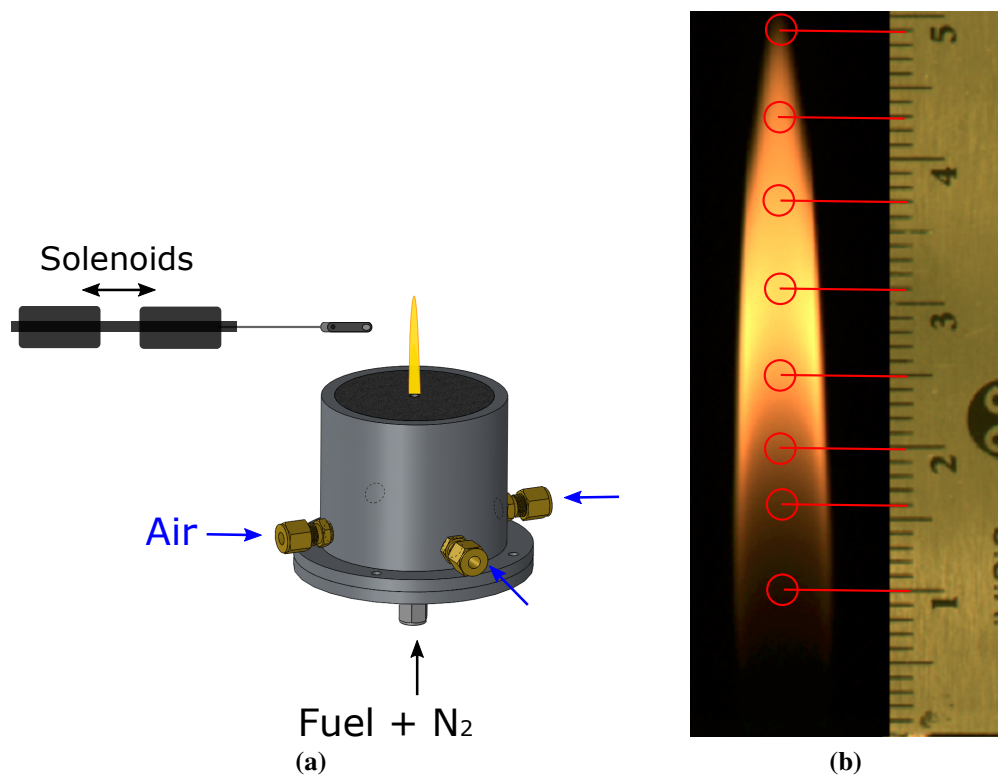


**Figure S1:** Representation of (a) the burner and fast-insertion sampling, and (b) the flame sampling positions

## A.2 Soot sampling

Soot was sampled using a fast-insertion thermophoretic sampling system [10]. The sampling instrument consists of two linear solenoids (MCSMT-3864S12STD, 12 VDC) connected to each other such that one pushes forward and the other backward. The system is controlled by a PLC that triggers each solenoid (at 30 V and 3 Amp) with a lag time in between, this time can be adjusted to change the exposure of the sampler in the flame. The sampler is mounted on one of the solenoids and consists of two metallic sheets used to hold the TEM grid. The design of the sampler was improved from our previous studies [10] according to the suggestions made by Lee and Yang [33] to minimise the flame disturbance. The aluminium sheet tongue inserted in the flame was trimmed to the minimum that allowed to hold the grid, to a width of 4 mm and thickness of 0.8 mm. A representation of the burner and sampling system can be seen in **Figure S1a**. The sampling probe was aligned parallel to the flow and offset 0.2 mm radially in order to best capture the particles at the centreline, as suggested by detail flow simulations performed by Kempema and Long [27] on a similar flame. The tongue was scrubbed with isopropanol and allowed to dry after each flame insertion in order to avoid cross-contamination between sample locations.

The sampling conditions were selected to minimise flame disturbance, contamination from other flame positions and grid coverage. The exposure time of the sampler and the disturbance of the flame during its fast insertion were analysed using a fast speed camera (1000 fps). It was found that the radial and axial vibration of the sampling probe had a great influence on the flame disturbance. A damper was used to minimise the vibration of the probe [34], resulting in a maximum vertical displacement of  $\pm 0.2$  mm and horizontal displacement of  $\pm 0.1$  mm.

In order to obtain a sample coverage below 15% and minimise the effect of contamination from the wings, different exposure times (20, 50, 100 and 200 ms) were evaluated at different HAB (13, 25 and 37 mm). Exposure times between 20 and 50 ms gave the best sample coverage for all HAB (max. 13% coverage). For all the sampling positions presented in this study, the exposure of the grids was between 30-46 ms. Contamination of the sample from large wing aggregates was estimated to be  $\pm 15\%$ . At lower HAB (10, 16, 20 and 25 mm) it was possible to detect these particles from different positions and eliminate them; unfortunately, at larger HAB the contamination could not be isolated. However, as HAB increases the differences in the aggregate and primary particle sizes between the wing and centreline are smaller, and therefore the induced error is also expected to be smaller [27]. At the tip of the flame (43 and 49 mm) the effect of contamination is considered negligible.

## B Numerical parameters

The following table lists the numerical parameters utilized in the detailed population balance model.

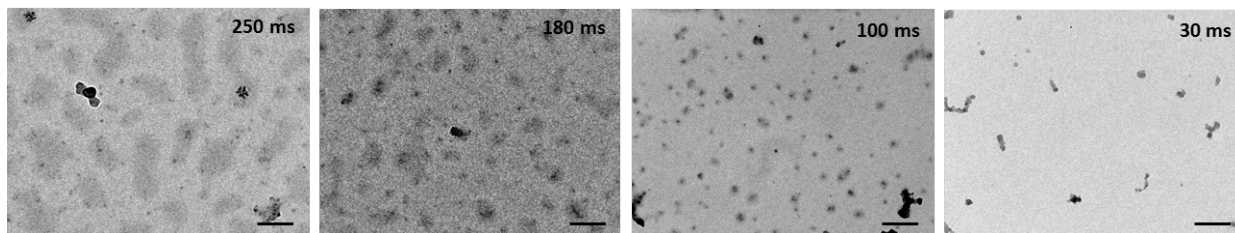


**Figure S2:** TEM images of soot sampled at 25 mm HAB and different exposure times. The calibration bar in the images correspond to 200 nm.

**Table 2:** Model parameters in detailed population balance model.

| Parameter  | Range   | Value                                  |
|--|---|--|
| 1) Minimum number of 6-member aromatic rings in a PAH for inception  | -   | 5                                      |
| 2) Minimum number of 6-member aromatic rings in a PAH for condensation   | -   | 5                                      |
| 3) Minimum number of 6-member aromatic rings in a PAH in a particle ( $n_{\text{PAHs}} \geq n_{\text{crit}}$ ) below which it is removed | -   | 4                                      |
| 4) Soot density, $\rho$  | $1 \text{ g cm}^{-3} \leq \rho \leq 2 \text{ g cm}^{-3}$            | $1.88 \text{ g cm}^{-3}$               |
| 5) Smoothing factor, $\sigma$  | $0 \leq \sigma \leq 2$  | 1.69                                   |
| 6) Growth factor, $g$  | $0 \leq g \leq 1$   | 0.15                                   |
| 7) Critical number of PAHs in a primary particle before the growth factor is applied, $n_{\text{crit}}$                                  | $\geq 2$  | 4                                      |
| 8) Sintering model:  |   |  |
| - $A_s$  | -   | $1.1 \times 10^{-14} \text{ s m}^{-1}$ |
| - $E_s$  | $1.8 \times 10^4 \text{ K} \leq E_s \leq 1.8 \times 10^5 \text{ K}$ | $9.61 \times 10^4 \text{ K}$           |
| - $d_{\text{p,crit}}$  | $1 \text{ nm} \leq d_{\text{p,crit}} \leq 5 \text{ nm}$             | 1.58 nm                                |

## C Sensitivity analysis of the soot model parameters

Sensitivity analysis of different parameters in the PPSD: sintering pre-factor, particle size threshold for coagulation and instantaneous coalescence, and smoothing factor.



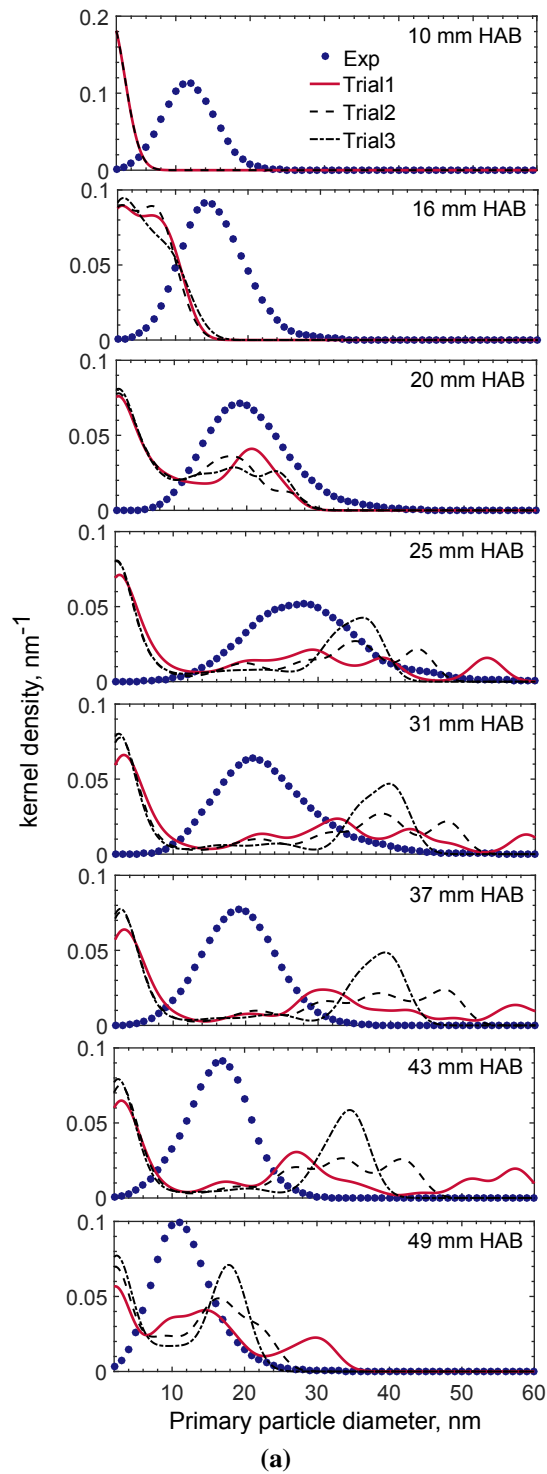


**Figure S3:** Primary particle size distribution sensitivity to sintering factor

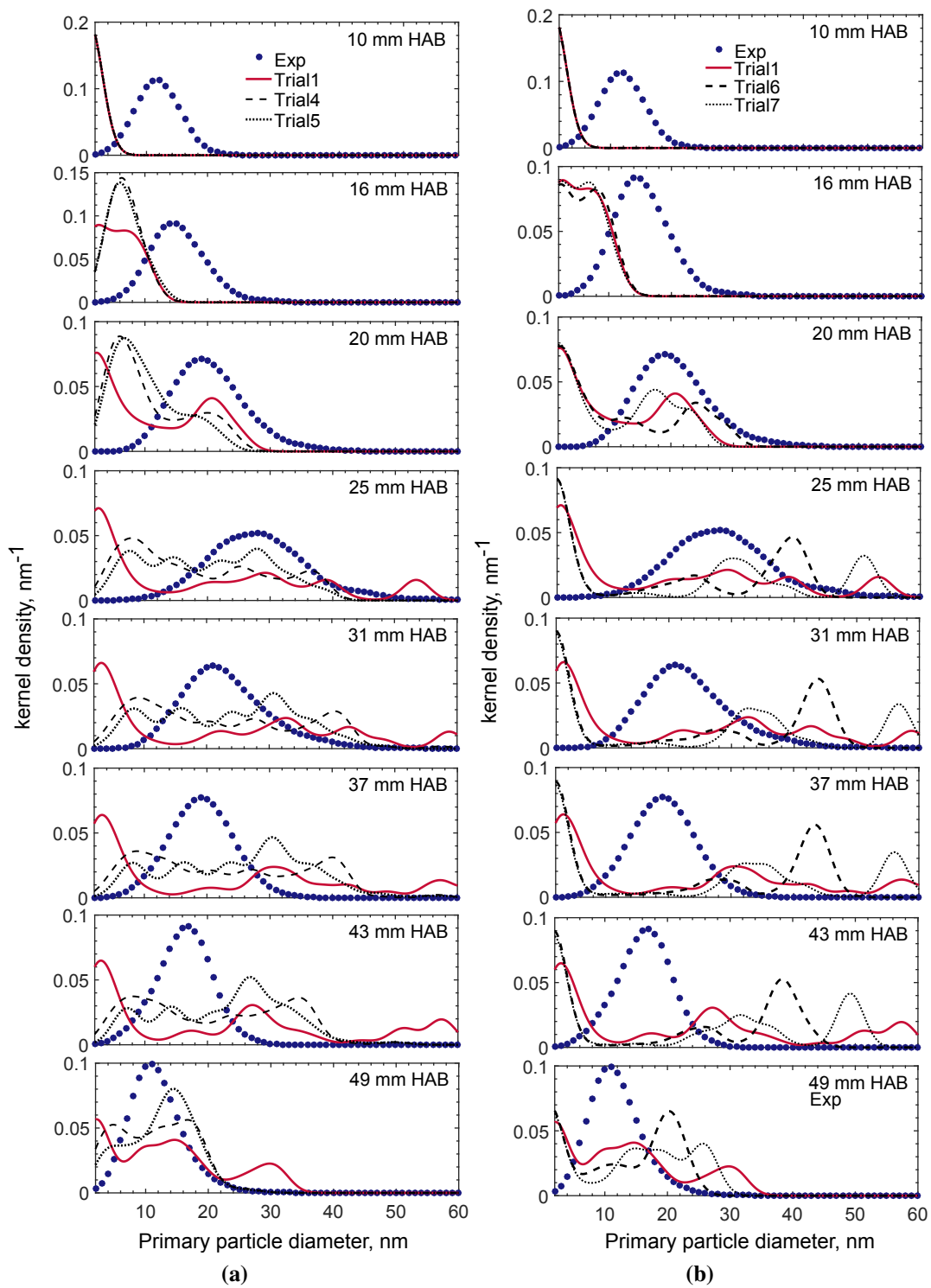


**Figure S4:** Primary particle size distribution sensitivity to (a) particle size threshold for coagulation and instantaneous coalescence and (b) smoothing factor